Research Article | Vol. 32, No. 27 / 30 Dec 2024 / Optics Express 48114
Optics EXPRESS

# High dioptric power micro-lenses fabricated by two-photon polymerization

BEHJAT S. KARIMAN,[1] ALESSANDRA NARDINI,[2] MARIO MARINI,[3] PABLO ROLDÁN-VARONA,[4] CLAUDIO CONCI,[2] MANUELA T. RAIMONDI,[2] ROBERTO OSELLAME,[5] GIULIO CERULLO,[1] GIUSEPPE CHIRICO,[3,*] AND REBECA MARTÍNEZ VÁZQUEZ[5]

[1]*Department of Physics, Politecnico di Milano, Milan, Italy*
[2]*Department of Chemistry, Materials and Chemical Engineering "Giulio Natta", Politecnico di Milano, Milan, Italy*
[3]*Department of Physics, Università degli Studi di Milano-Bicocca, Milan, Italy*
[4]*Institute of Photonics and Quantum Sciences, Heriot-Watt University, Edinburgh, EH144AS, UK*
[5]*Institute for Photonic and Nanotechnologies (IFN), CNR, Milan, Italy*
[*]*giuseppe.chirico@unimib.it*

**Abstract:** Specimen-induced aberrations limit the penetration depth of standard optical imaging techniques in vivo, mainly due to the propagation of high NA beams in a non-homogenous medium. Overcoming these limitations requires complex optical imaging systems and techniques. Implantable high NA micro-optics can be a solution to tissue induced spherical aberrations, but in order to be implanted, they need to have reduced complexity, offering a lower surface to the host immune reaction. Here, we design, fabricate, and test a single micro-optical element with high dioptric power and high NA (up to 1.25 in water). The sag function is inspired by the classical metalens phase and improved to reduce the spherical aberrations arising from the refractive origin of the phase delay at the lens periphery. We successfully fabricated these high-NA quasi-parabolic aspheric microlenses with varying focal lengths by two-photon polymerization in biocompatible photoresist SZ2080. The entire process is optimized to minimize fabrication time while maintaining the structures' robustness: the smoothness reaches optical ($\frac{\lambda}{20}$) quality. The dioptric power and magnification of the microlenses were quantified over a $200 \times 200$ µm aberration-free field of view. Our results indicate that these microlenses can be used for wide-field imaging under linear excitation and have the optical quality to be utilized for nonlinear excitation imaging. Moreover, being made of biocompatible photoresist, they can be implanted close to the observation volume and help to reduce the spherical aberration of laser beams penetrating living tissues.



## 1. Introduction

The multiple light scattering observed in biological tissues poses a significant challenge to optical biomedical imaging. It restricts the penetration depth for most optical imaging techniques by attenuating the incident light intensity and reducing the signal contrast by a diffuse background noise [1]. There are two main approaches to increase the signal contrast at the sample plane. One is to exploit wavelengths falling in short-wave infrared (SWIR) region (1-2 µm) of the spectrum, for which the tissue scattering decreases substantially with respect to the visible range. By carefully avoiding the local maxima of the water absorption spectrum, substantial reduction of radiation scattering can be obtained with low thermal load [2]. In these spectral range, one can exploit the highly localized non-linear absorption or scattering, to obtain label-free 3D visualization of different tissue components. Label-free non-linear excitation approaches comprise second- and third-harmonic generation (SHG/THG), two-photon excitation fluorescence (TPEF), transient absorption, stimulated Raman scattering (SRS), and others [3,4], all of which

#545139 https://doi.org/10.1364/OE.545139
Journal © 2024 Received 17 Oct 2024; revised 17 Nov 2024; accepted 19 Nov 2024; published 17 Dec 2024

Optics EXPRESS

require tightly focused, high numerical aperture (NA) excitation beams. The second approach is to use adaptive optical strategies to correct the aberrations induced by the inhomogeneous tissue on the propagating light waves [5]. In fact, the major optical aberration arising from propagation into tissue is the spherical one, closely related to the propagation of highly focused beams (high NA) in inhomogeneous media. Conventional Adaptive Optics (AO) methods based on a description of the wave distortion with smooth Zernike or similar polynomials can correct these types of sample-induced aberrations but are lengthy and limit the possibility of continuous monitoring of the biological function offered by optical microscopy. The situation worsens if we consider also the random distortion of the wave phase due to scattering in the tissue that can be corrected with phase inversion methods [6].

These two widely used approaches are linked in a negative feedback. In fact, the use of non-linear excitation microscopy is beneficial in reducing the tissue scattering since it employs light in SWIR region of the spectrum [7]. However, nonlinear excitation requires high intensities that can only be achieved with a tightly focused, undistorted laser beam at the sample plane, since the signal arising from two- or three-photon excitation scales steeply with the NA of the objective, $\approx NA^4$ and $\approx NA^6$, respectively. The use of high NA optics, on the other hand, increases spherical aberrations on the beam that propagates in the inhomogeneous biological tissue. To disrupt this harmful cycle, we here envisage high NA micro-optics that can be placed as close as possible to the observation volume, implanted in the tissue. By entering the tissue with a quasi-collimated beam and focusing it very close to the sample, we could then reduce a good fraction of the detrimental tissue effect on the beam phase.

The trend towards miniaturization of devices is making micro-optics a unique enabling technology for many optical products and applications today, playing a crucial role in biomedical devices, bio-imaging, or fiber communication networks, among others [8,9]. Over the last decades, using high NA micro-lenses individually or multiplexed in an array allowed for high-resolution imaging and high signal-to-noise-ratio detection in micro-optical and integrated optics applications [10–12].

Among available processing techniques for developing micro-optics, two-photon polymerization (2PP) allows the fabrication of arbitrarily complex 3D micro/nanostructures with surface roughness suitable for optical applications without subsequent polishing [13–16]. In fact, the intrinsic high spatial resolution of 2PP allows for the manufacturing of intricate three-dimensional freeform surfaces [17]. A parametrization of the scanning path for fabrication as a function of the lens profile [13] enables optimization of the surface optical quality. However, the high spatial resolution of 2PP is intrinsically linked to a low throughput due to its serial nature, not suitable for the fabrication of large-scale volumetric elements. To speed up the fabrication process and mechanically strengthen the final structure, it is possible to use an approach consisting of irradiating only the outer shell of the structure, followed by the cross-linking of the unpolymerized inner core through a fast post-fabrication UV exposure [18,19]. Despite significantly reducing fabrication time and producing stable high-quality refractive-diffractive elements, this method remains confined to small-scale components, typically tens of microns in size. The main limitations associated with the production of the most common optical systems lay in fact, in restrictions in shape and size related to the intrinsic features of the manufacturing techniques [20,21]. For widefield imaging over large angles and with high numerical apertures, complex shapes for aberration corrections are often required.

Recently, lens fabrication has benefited from 2PP's capability to produce complex three-dimensional structures with smooth surfaces, enabling the creation of single and multiplex optics [22]. As reported by Gissibl *et al.*, the fabrication of an ultracompact multi-lens system with various refractive indexes using femtosecond 2PP demonstrates the capabilities of this additive manufacturing method for creating complex high-quality multi-elements lenses showing one of the highest NAs ever produced of 0.3 [21]. The same group complementarily showed the

Optics EXPRESS

potential to combine freeform optics with three-dimensional femtosecond printing to fabricate sub-μm optical components directly on optical fibers [20]. Beyond traditional refractive optics, researchers have focused on three-dimensional diffractive devices [23]. For example, Thiele *et al.* developed doublet and triplet diffractive elements with a good field of view (FOV) in the visible range, fabricated in less than 15 minutes [24]. Recently, the pursuit of ultra-thin, ultra-compact, and multipurpose optical systems has brought metalenses to the forefront, expanding applications from integrated circuits and quantum technology to enhancing imaging quality in the biomedical field. Bali *et al.* for instance, presented multi-level diffractive lenses combined with metalenses to create a high efficiency hybrid achromatic metalens operating in the near infrared band [25]. However, the micro-optics developed in all these studies cannot be easily employed in tissues for a number of reasons. Despite the high NA they can reach, their size limits the FOV and therefore the observation of relevant portion of the tissue. Moreover, the complexity of the proposed optical elements (refractive triplets or metalenses) with small size interstices between the optical elements, hinders the possibility of direct implant by triggering inflammatory response from the tissue [26,27]. Finally, the shape of the proposed micro-optical element should be tailored on the specific properties of the tissue in which they are implanted, implying the repetition of a lengthy numerical design and fabrication procedure.

In this work we present single-element micro-optics, with high NA and a few hundred μm FOVs, fabricated by 2PP. Refractive lenses based on the conventional plano-spherical shape cannot be used for FOV larger than twice the radius of curvature of the lens, which is relatively small for high dioptric power and NA. Moreover, the height of the lens intrinsically growths with the NA, thus posing several problems for the fabrication by 2PP. To overcome these limitations, we present a novel design based on a quasi-parabolic aspheric shape of the curved surface, with the sag function inspired to the classical metalens phase and improved to reduce the spherical aberrations arising from the refractive origin of the phase delay at the lens periphery. Our design allows us to obtain 600 μm diameter microlenses, with high NA (≃1.25 in water) and large FOV (≃200 μm) and a single tunable physical parameter. We demonstrate the feasibility of 2PP for fabricating such large lenses in a fast and reproducible way, with an excellent surface quality. We further validate our approach by performing morphological and optical characterization of these lenses. Finally, we evaluate the optical performance of our high-NA microlenses as complementary imaging elements using the linear excitation mode. In the future, we envisage the possibility of using them as molds for fast lens replication and also as implanted optical elements to increase the performance of *in vivo* nonlinear bio-imaging.

## 2. Result and discussion

The novel lens design is inspired by the phase of parabolic meta lenses, that allow to obtain high dioptric power lenses with focal lengths in the micrometer range, keeping a simple optical design. Moreover, the relatively low height of these lenses, compared to the conventional plano-convex ones with similar NA, permits to use a fast protocol for the 2PP fabrication, maintaining an excellent accuracy for the lens profile and low roughness without losing the stability of the 3D structure during the process. A careful characterization of their morphology and optical properties, with particular attention to the point spread function (PSF) and optical phase, demonstrates the goodness of our approach. Finally, the wide-field imaging capabilities of the microlenses are presented, demonstrating the optimal imaging properties of the lenses and the high FOV.

### 2.1. Design of quasi-parabolic microlenses

With a spherical plano-convex lens it is not possible to have high numerical aperture (or high magnification) for low focal lengths. Indeed, if we consider a planoconvex spherical lens with radius of curvature R, fabricated in a medium with refractive index $n_L$, the maximum size of the

Optics EXPRESS

lens is 2R and its effective focal length is defined by

$$EFL = \frac{R}{(n_L - 1)}\left(1 + \frac{(n_L - 1)^2}{n_L}\right) \tag{1}$$

For $n_L \simeq 1.5$,

$$EFL \simeq \frac{R}{(n_L - 1)} \simeq 2R \tag{2}$$

If we require to image a sample very close to the microlens, *i.e.* 200 μm or less, R should be about 100 μm . However, since the impact of optical aberrations on the imaging FOV follows a well-known scaling law [28], the use of such a small lens inherently limits the space-bandwidth product of the optical system .

We propose an innovative approach to enlarge a single lens FOV, while maintaining short focal lengths. We keep a plano-convex configuration with a different shape for the curved surface inspired to the parabolic shape originally used to design metalenses [29]. These metalenses are designed to imprint on the wave front an excess phase with a profile $\Phi\ (r) = f - \sqrt{(f^2 + r^2)}$, that ensure that a collimated beam is exactly focused at a distance $f$ from lens along the optical axis in any uniform medium, without spherical aberrations. For refractive lenses of thickness $H_{tot}$, as in this case, we can first adopt the following sag function:

$$z_1(r) = H_{tot} - \left(\sqrt{f_n^2 + r^2} - f_n\right) \tag{3}$$

The parameter $f_n$ is not anymore equal to the focal length and the dioptric power depends on the refractive index of the lens and its difference with the refractive index of the surrounding medium (see Supplement 1, S1, "focal length of a parabolic refractive lens"). Moreover, the sag shape $z_1(r)$ implies spherical aberrations when used with refractive materials. To limit this drawback, we have applied a slight change to the sag function $z_1(r)$ (see Supplement 1, S1) that reduces the excess phase of the marginal rays in the refractive element:

$$z_2(r) = H_{tot} - \left(\sqrt{f_n^2 + r^2} - f_n\right)\sqrt{1 + \left(\frac{r}{f_n}\right)^2} \tag{4}$$

Notably, Eq. (4) is a parametric description of the lens curved surface that is defined for any value of the radial coordinate $r$, not being limited to $r \leq EFL/2$. We can therefore increase at the same time the FOV and the numerical aperture with respect to the plano-convex lens, with limited spherical aberrations.

The optical behavior of the quasi-parabolic microlenses was studied using the sequential mode of Zemax OpticStudio (Ansys corp. USA). We chose to work with a diameter of 600 μm, wide enough to provide a FOV of the order of 300 μm, comparable with the FOV obtained on confocal and non-linear excitation microscopes [30,31]. We explored the set of nominal focal lengths $f_n$ = 250, 300, 350 *and* 400 μm (Fig. S2.1(a)), which correspond to thicknesses of the resulting aspherical lenses of $H_{dome}$= 207, 172, 146, and 125 μm, respectively. To this value, we must add a thin pedestal layer ($H_{pedestal}$ = 10 μm) that facilitates the attachment of the fabricated structure to the borosilicate substrate ($H_{substrate}$ = 170 μm). These thick lenses have one principal plane coincident with the position of the vertex of the curved surface and a second one inside the microlens. As an example, the optical design of a $f_n$ = 350 μm microlens, and the location of its principal planes is shown in Fig. 1. Figure 1(a) and (b) display the 3D, and 2D sketch of this parabolic microlens based on sag parabolic function given by Eq. (4), respectively.

Optics EXPRESS

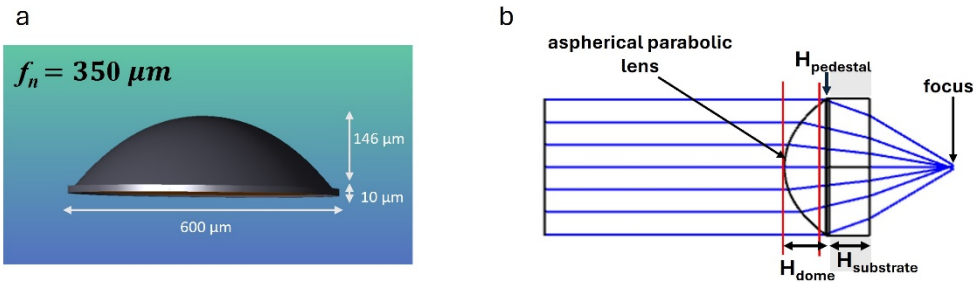


**Fig. 1.** Design and simulation of parabolic microlenses with diameters of 600 µm by Zemax Optic studio. (a) 3D sketch of the parabolic lens ($f_n$ = 350 µm) and (b) Optical design of the single aspherical parabolic microlens fabricated on a N-BK7 glass substrate with $H_{substrate}$ = 170 µm thickness. The red vertical lines indicate the positions of the principal planes.

### 2.2. *Fabrication of quasi-parabolic microlenses*

The parabolic microlenses were fabricated on top of a supporting borosilicate glass ($H_{substrate}$ = 170 µm) by the 2PP of the SZ2080, a biocompatible hybrid organic-inorganic photoresist with good mechanical properties and low shrinkage [17,32,33,34]. This choice was particularly relevant here to ensure the possibility to fabricate wide suspended domes with well reproducible size. To reduce the fabrication time of the micro-optics, given their relatively high volume, we utilized a µm-sized 2PP voxel to structure the outer shell of the lens followed by UV polymerization of the inner volume [10]. Precisely, the parabolic shell is two-photon polymerized by directly irradiating the photoresist droplet with the laser beam, by a continuous helical scanning of the surface, which decreases in radius along the lens optical axis (Fig. 2(a)). This continuous helical trajectory optimizes the fabrication, eliminating waiting times associated with mechanical or software delays, with a smooth transition between different lens heights. To ensure the desired resolution and suitable overlap of the polymerized lines, the height map of the lens is resampled using radial (dR) and vertical (dZ) steps of 0.25 µm and 0.75 µm, respectively. The irradiation parameters were then optimized to minimize superficial roughness and inhomogeneity, especially in the upper central part of the parabolic lens. More specifically, we implemented a "gray scale like" approach by gradually decreasing the writing velocity and laser power. We have reduced the speed at the central area of the top of the lens from 1 mm/s to 0.4 mm/s. This reduction starts at a specific radial position ($R_{decr}$), and we have further decreased the power by around 5-10% to ensure uniform absorption of the laser pulses throughout the structure. The suitable radial position has been selected based on the design of the parabolic lens. For example, $R_{decr}$ = 8 µm was set for $f_n$ = 350 µm, corresponding to a lens height of 141 µm. (Figure 2(a)). Furthermore, by decreasing the speed, the instability of the stages is limited when approaching the top of the lens, where the scanning radius of the lens become extremely small. After obtaining the 2PP structured parabolic shell, the entire sample undergoes a development process in an alcoholic solution for approximately 30 minutes to remove the surrounding unpolymerized photoresist. At this stage, the inner unpolymerized core of the lens is crosslinked in bulk by exposing the entire sample to UV irradiation with wavelength $\lambda$ = 385 nm, and the dose = 36 J for each step. Following our previous work [10], UV exposure is conducted by passing light through the glass substrate to avoid direct exposure of the previously polymerized surface. The exposure conditions strongly depend on the substrate thickness, the volume of the photoresist being polymerized, and the shape of the lens. Indeed, for these lenses we developed a 3D UV irradiation process with three steps at different incident angles ($0^o, -45^o, +45^o$) to achieve high stability for the final lenses (Fig. 2(b)). A normal UV irradiation only at $0^o$ incidence resulted in unstable lenses

Optics EXPRESS

that collapsed during standard handling (see Supplement 1 Fig. S3.1(a)). This optimization ensured highly stable quasi-parabolic lenses, demonstrating the reliability of the overall process for any value of the lens focal lengths, as illustrated in Fig. 2(c) that shows the Scanning Electron Microscopy (SEM) image of 4 fabricated parabolic microlenses with nominal focal lengths $f_n$ = 250 , 300, 350 and 400 μm. The different heights of the lenses depending on $f_n$ and their superficial quality are clearly visible.

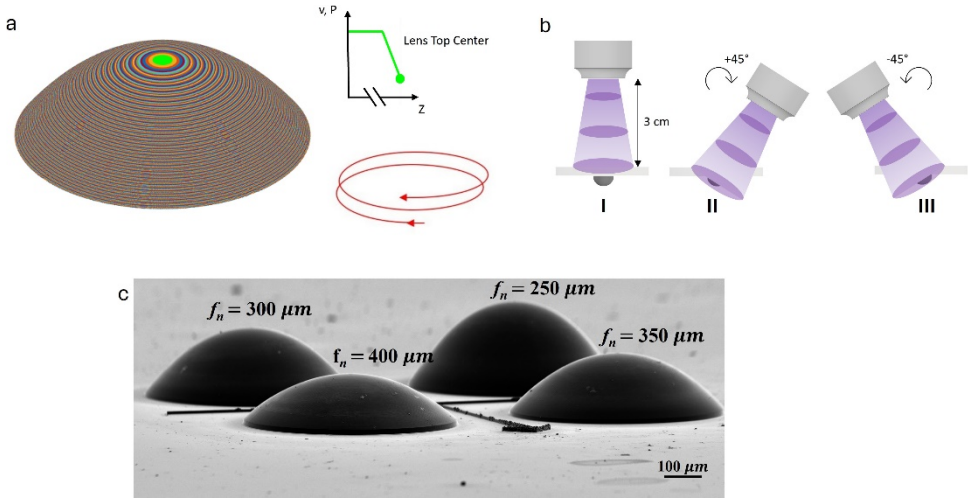


**Fig. 2.** Scheme of the microlenses fabrication with diameter Ø = 600 μm. (a) Microlens outer shell 2PP inscription procedure (b) UV exposure to cross-link unpolymerized core of the lens in three steps at different angles ($0^o$, $-45^o$, $+45^o$), respectively. At each step the sample is illuminated with 50% of intensity for 40 seconds (c) SEM images of 4 single parabolic microlenses with variable nominal focal lengths (250 , 300, 350 and 400 μm) respectively, which were fabricated on a cover-slide with a thickness of 170 μm.

### 2.3. *Surface characterization by scanning electron microscopy and optical profilometer*

The hybrid 2PP-UV curing fabrication protocol was carefully optimized to obtain the smoothest surface for fabricated parabolic microlenses. The quality, shape, and morphological characterization of microlenses were evaluated by SEM as shown in Fig. 3(a), 3(b) and 3(c). Moreover, the zoomed central region on the top plane of the lens in (b) indicates the improved surface optical quality achieved by this newly developed 2PP process compared to our previous work [10]. The height of the pedestal measured on the SEM images was 10 ±0.1 μm for all the fabricated microlenses, in very good agreement with the technical drawing (Fig. 1(a)). On the same SEM images, we could also quantify the height of the curved surface finding $H_{dome}$ =233.8± 0.1, 186.6 ± 0.1, 151.6± 0.1, and 131.3 ± 0.1μm for parabolic microlens at $f_n$ = 250, 300, 350, and 400μm, respectively (see also Fig. S3.2(a)). Table 1 summarizes the design heights of all the parabolic microlenses together with the retrieved experimental values, it should be pointed out that no pre-compensation of lens profile is applied during lens design. We obtain the largest discrepancy in height, of about 8%, for the $f_n$ = 250μm lens, which is also the tallest one. For the other lenses the discrepancy is lower than 2%. We can hypothesize that during the 2PP of the $f_n$ = 250μm lens the thickness of the polymerized voxel increases due to aberrations, as the lens is rather high and consequently the laser irradiation of the top part of the lens is performed through a thickness of photoresist that is lower than the value for which the objective is compensated [35], but a deeper study of voxel dimension would be required to demonstrate it.

Optics EXPRESS

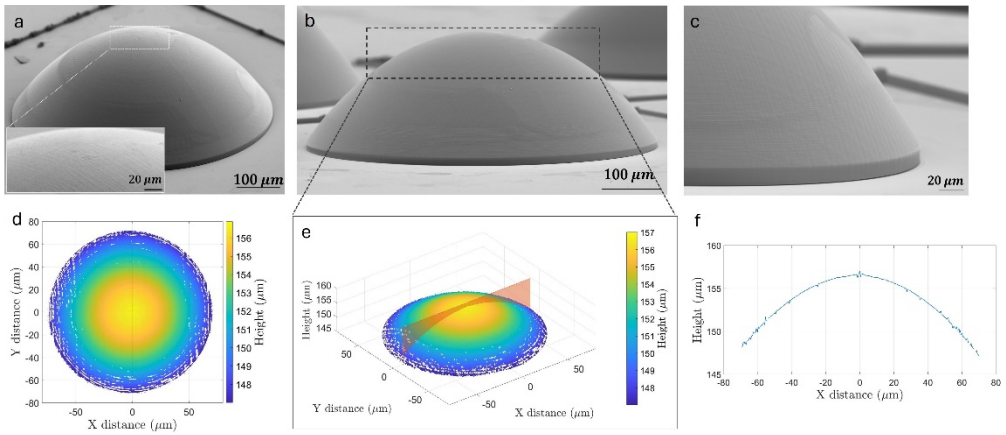


**Fig. 3.** Shape and surface characterization employing SEM and 3D optical profilometer. (a), (b), and (c) SEM images of a single parabolic microlens with diameter Ø = 600 μm, and $f_n$ = 350 μm. Close up of the central region on the top plane of the lens of (a) highlights the improved smoothness obtained in our fabrication process. (d) 2D optical profiles over a topographic area = 229 × 172 μm$^2$ of top of the lens in panel (b). (e) 3D optical profiles over a topographic volume = 229 × 172 × 60 μm$^3$, covering the central region on the top dome of the lens in panel (b). (f) The scan length was 101 μm, and the 2D line profile was acquired over a distance of 165 μm along the x-axis and 31.15 μm along the z-axis, starting from the top of the lens and moving downwards. The average line roughness of $R_a \approx 24.0 \pm 4$ nm was obtained.

**Table 1. Geometrical parameters of parabolic microlenses with variable nominal focal lengths[a]**

| $f_n$ (μm) | $H_{dome}$ | $H_{pedestal}$ | $H_{tot}$[μm] | $H_{meas}$[μm] | $\Delta H$% |
|---|---|---|---|---|---|
| 250 | 207 | 10 | 217 | 233.8 ± 0.1 | 7.7 |
| 300 | 172 | 10 | 182 | 186.6 ± 0.1 | 2.5 |
| 350 | 146 | 10 | 156 | 157.4 ± 0.1 | 0.9 |
| 400 | 125 | 10 | 135 | 138.2 ± 0.1 | 2.3 |

[a]The total height of the microlenses is made up of the height of the curved dome ($H_{dome}$), the pedestal ($H_{pedestal}$) and the thickness of the substrate which is 170 μm. These parameters are reported in Fig.1b. All the values are in μm. The total height of the microlenses ($H_{tot}$) is the design value. The values measured from SEM images (see Supplement 1) are reported in the last column. $\Delta H$ represents the difference between theoretical and experimental values of $H_{meas}$.

For optical imaging, the gold standard for surface roughness is $< \frac{\lambda}{20}$. Therefore, apart from the visualization of the surface smoothness done by SEM (Fig. 3(a)-(c)), we accurately measured the surface topography of our microlenses by means of an optical profilometer with the highest magnification objective lens [36]. Figure. 3(d), and 3(e) show the 2D, and 3D profile associated to the top part of the $f_n$ = 350 μm lens (Fig. 3(b)). The area and volume measured were as follows: area = 229 × 172μm$^2$, and 229 × 172 × 60μm$^3$ in the X, Y and Z axis respectively. The 2D section of this microtopography, at the central Y axis position (0 μm), provides an average line roughness of $R_a \approx 24.0 \pm 4$ nm based on 560 sampled points (Fig. 3(f)). This value highlights the efficiency of the fabrication process in achieving high surface smoothness. Additionally, an overall surface roughness of $S_a \approx 22.7 \pm 3.3$nm was obtained for an area of 45 × 45 μm$^2$ on top central part of lens employing high-frequency filtering (see S4). This value corresponds

Optics EXPRESS

to $\simeq\lambda/26$, for a 633 nm wavelength, which is lower than the optical gold standard and thus demonstrates the good optical quality of the surfaces fabricated by means of our protocols.

### 2.4. Optical characterization

After the morphological characterization we made a complete study of the optical properties of the fabricated lenses. In the following we present the details for the $f_n$ = 350 μm lens as an example. Data for all the lenses are reported in the Supplement 1 (Table S5.1).

In an initial investigation of optical quality, we determined the back focal length and PSF by illuminating them with a collimated laser beam under overfilling conditions. To assess the microlens behavior in the visible region this characterization was performed at three different wavelengths $\lambda_1 = 473$, $\lambda_2 = 532$, and $\lambda_3 = 638$ nm (Fig. 4(a)). The intensity distribution on planes perpendicular to the optical axis was sampled at 5 μm steps along the optical axis, in a range of ±80 μm around the effective focal plane of the microlenses (corresponding to the minimum spot size of the beam). Figure 4(b) reports five of these images at different positions along the optical axis, as an example.

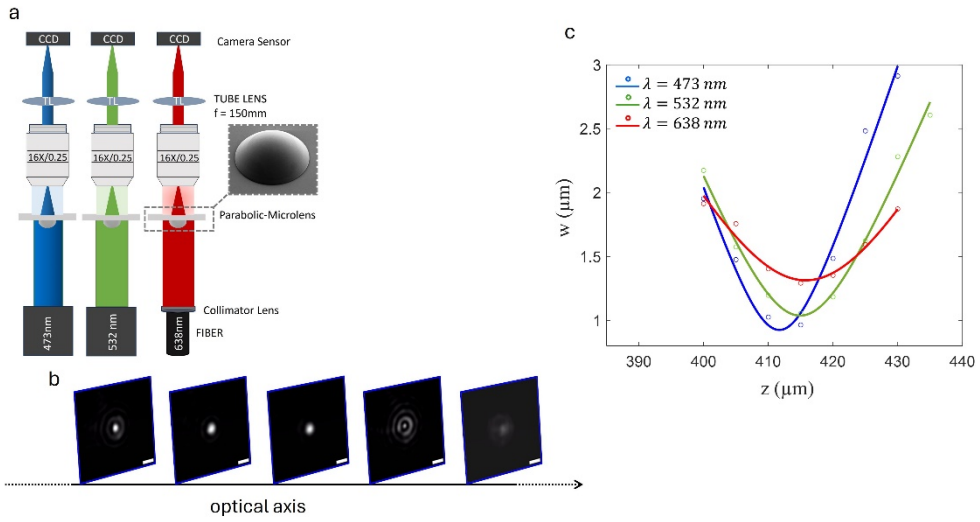


**Fig. 4.** Measurement of the beam profile through a $f_n$ = 350 μm microlens (diameter Ø = 600μm) for three different wavelengths. (a) The scheme of optical characterization setup. (b) Image intensity profiles collected along the optical axis at wavelength = 473 nm, in which the interplane distance of images is 15 μm. Scale bar 4 μm. The images of intensity distribution were acquired around the effective focal plane of microlenses from left to right. (c) The plot of measured $1/e^2$ beam size (w) as a function of the optical axis (z) (dot), which are measured by cumulative sum of intensity profiles, and fitted (solid line) by Eq. (5) at wavelengths 473 nm, 532 nm, and 638 nm, respectively.

We can obtain the beam waist at each plane perpendicular to the optical axis, w(z), by computing the cumulative sum of the beam intensity distribution along the columns of the image and fitting it to an error function [37], whose free fitting parameter is the beam waist. The points in the graph in Fig. 4(c) correspond to the best fit values of the beam waist obtained by fitting the cumulative sum to the error function. The waist $\left(\frac{1}{e^2}\ \text{radius}\right)$ of an ideal Gaussian beam focused along the optical axis is related to its Rayleigh range ($z_R$) and focal length by the relation:

$$w(z) = w_0\sqrt{1+\left(\frac{z-f}{z_R}\right)^2} \tag{5}$$

Optics EXPRESS

**Table 2. Comparison of the experimental to the simulated values of the back focal lengths[a]**

| | ($\lambda_1$ = 473nm) | | ($\lambda_2$ = 532nm) | | ($\lambda_3$ = 638nm) | |
|---|---|---|---|---|---|---|
| | Back Focal length (μm) | | Back Focal length (μm) | | Back Focal length (μm) | |
| Parabolic $f_n$ (μm) | Theory | Experimental | Theory | Experimental | Theory | Experimental |
| 250 | 288±9 | 204 ±9 | 287±9 | 206 ±9 | 287±9 | 207 ±13 |
| 300 | 333 ± 9 | 301 ± 4 | 337±9 | 302 ± 6 | 342 ±10 | 310 ± 6 |
| 350 | 440 ± 9 | 407±4 | 439±10 | 411±5 | 439 ±10 | 413±5 |
| 400 | 543 ±10 | 511±4 | 541±10 | 513 ± 2 | 542 ±10 | 518 ±5 |

[a]Comparison of the experimental to the simulated values of the back focal lengths (BFL) for microlenses with diameter = 600 μm, and $f_n$ = 250, 300, 350, and 400 μm).

The best fits of the beam waist to Eq. (5) at each plane along the optical (z) axis are shown, as solid lines, in Fig. 4(c) for the three wavelengths From these fittings we obtain the values of the diffraction limit of the beam waist and of the back focal lengths; those for the $f_n$ = 350 μm lens are $w_0$ = 1.3 ± 0.3 , 1.06. ± 0.1, 1.2 ± 0.1 μm and $f$ = 407 ± 4 , 411 ± 5, 413 ± 5 μm for $\lambda$ = 473, 532, and 638 nm, respectively. The acquired images reveal the presence of minor spherical aberrations as concentric circles, more evident on planes lying beyond the focal spot, as expected from the physical treatment of aberrations [38]. The experimental focal lengths for the different wavelengths are almost identical, even though a systematic increase is observed going from blue to red, as expected. The small variation observed, that lies within the experimental uncertainty, suggests a large Abbe number ($V_A$) for SZ2080. Indeed, from the measurement of the SZ2080 refractive index with the addition of photoinitiators [32], we can estimate a value $V_A \simeq 44$. The inverse of the Abbe number is approximately equal to the relative variation of the focal length over the visible range. The literature prediction $\frac{1}{V_A} \simeq 2\%$, compares favorably with our experimental result $\frac{BFL(\lambda_3)-BFL(\lambda_1)}{BFL(\lambda_2)} \simeq 1.6 \pm 0.4\%$. We can thus consider negligible the chromatic aberrations of the fabricated microlenses.

The experimental focal lengths measured were slightly lower than the focal length obtained from the Zemax simulations (Table 2). For $f_n$ = 250 μm, we observed a larger difference between theoretical and experimental focal length values, as for the measured height of the fabricated microlens. This difference might be attributed to a different refractive index of our 2PP + UV polymerized photoresist compared to SZ2080 polymerized in absence of photo-initiator [39]. Indeed, our simulations were run with the values $n_{SZ2080}$ = 1.47 and $n_{glass}$ = 1.5 for the photoresist and the glass respectively, as found in the literature [32]. Interestingly, the same calculation for a lens with refractive index = 1.53 gives a focal length very close to more recent experimental values [39] (see Table S5.2). It is worth noting that the refractive index of the photoresist varies during the polymerization process and UV exposure, resulting in changes in the final refractive index of the fabricated microlenses [16,40]. It is noteworthy that the slightly greater height of the final fabricated lenses compared to the simulated ones, does not explain the deviations of the focal length from the expected values. Instead, the use of a slightly higher value of the refractive index is responsible for the deviations.

To assess the uniformity of the polymerized resist throughout the volume of the microlens, we directly measured the phase of the wave front emerging from the microlenses by means of off-axis digital holography microscopy (DHM). The setup is depicted in Fig. 5(a). As described recently for the characterization of metalenses [41], off-axis DHM allows the reconstruction of the whole phase profile of the lens (Fig. (5(b))). Once the full field phase and amplitude is reconstructed, one can compute all the optical response functions.

Optics EXPRESS

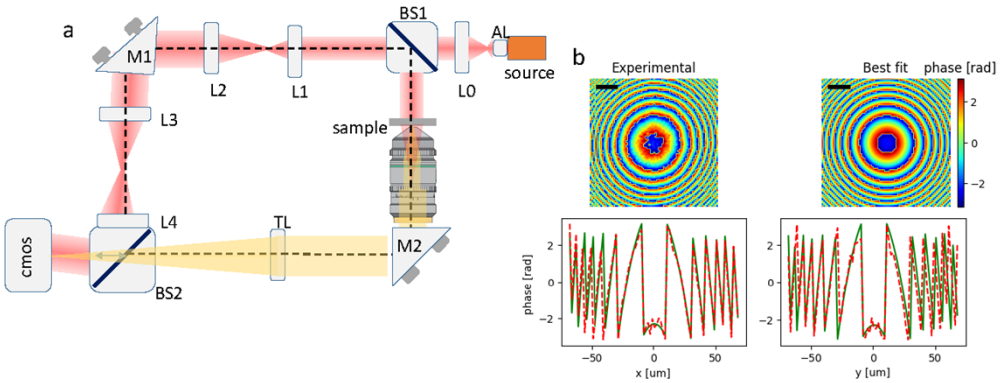


**Fig. 5.** (a) off-axis DHM setup used for the measurement of the microlens phase. A laser diode emitting at $\lambda = 635$ nm nm is expanded by a first beam expander (AL + L0 lenses). On the upper (reference) path, the beam is further expanded 2 times (L1 + L2 lenses) onto the mirror M1. A third telescope composed of the lenses L3 and L4 conjugates M1 onto the CMOS camera (IDS, UI-3240CP-M-GL). By tilting M1 along one axis, the reference beam impinges centered on the CMOS camera with a twofold angular demagnification. The lower (sample) path conjugates the sample plane (here the exit pupil of the microlens) onto the CMOS camera by means of the tube lens (TL) on the bottom path. The light field from the sample is superimposed with the reference beam on the camera. (b) results of the analysis of the phase profile for the $f_n = 350$ μm microlens over an area of $120 \times 120$ μm$^2$. The top images are the experimental phase computed from the DHM interferogram with a spatial resolution of 1.72 μm (left) and the best fit phase (right). The bars are 25 μm. The bottom plots are cross sections along the rows and the columns of the experimental (red dotted lines) and the best fit (green solid lines) of the phase images.

The interferogram of the exit pupil of the microlens was captured by the camera superimposed with the reference beam tilted by 0.035 rad with respect to the optical axis. The complex electric field was derived from the inverse Fourier transform over a region of interest, of the spatial Fourier transform of the interferogram obtaining a spatial resolution of 1.72 μm. This resolution was enough to recover the phase over at least $20 \times 2\pi$ rad. It is worth noting the remarkable regularity of the circular fringes that map the phase delay as a function of the radial distance, a fact that indicates the high uniformity of the polymerization protocol. The experimental phase was fit to the trial function:

$$\Phi_{trial}(r) = b - \frac{2\pi}{\lambda}(n_L - 1)\left(\sqrt{f_{fit}^2 + r^2} - f_n\right)\sqrt{1 + \left(\frac{r}{f_{fit}}\right)^2} \tag{6}$$

The baseline, b, is introduced to consider a slight mismatch in the path lengths over the reference and the sample paths. Its effect is clearly visible in the plots of Fig. 5(b) as a vertical shift of the central maximum of the recovered phase. The result of this analysis is summarized in Table 3.

### 2.5. *Wide-field imaging through microlenses*

To verify the imaging performance, microlenses were coupled to a wide-field microscope to acquire images both in transmission and in epi-fluorescence mode (see Materials and Methods 2.7).

We used the microlenses to image an USAF 1951 target both in virtual imaging configuration (Fig. 6) and in finite conjugate configuration (Fig. S6.1). In virtual configuration, the microlenses are positioned closer to the objective than its focal length. This coupling allows the microlenses

Optics EXPRESS

**Table 3. Result of the analysis of the DHM interferograms of the microlenses[a]**

| $f_n$(μm) | $f_{fit}$ (μm) | $b_{fit}$[rad] |
|---|---|---|
| 250 | 255 ± 5 | −1.7 ± 0.3 |
| 300 | 279 ±. 5 | +0.2 ± 0.1 |
| 350 | 331 ± 2 | +2.1 ± 0.1 |
| 400 | 393 ± 4 | +1.4 ± 0.1 |

[a]Best fit values of the parameters f, b of the phase shift described by Eq. (6) for microlenses fabricated with nominal values $f_n$. A value of the index of refraction = 1.46 [32] was adopted to fit the phase maps.

to alter the dioptric power and magnification properties of the objective, effectively serving as the final optical element of the entire system, a configuration similar to the application of these microlenses in in-vivo microscopy. The qualitative results of imaging in virtual mode, reported in Fig. 6(a)-(c), were obtained by coupling the microlens with 20x microscope objectives having numerical apertures of 0.4, 0.71 and 0.95 (water immersion). In all three optical configurations, the magnification of the total system is greater than that of the objective alone, with the microlenses having a more pronounced effect in systems with lower NA microscope objectives.

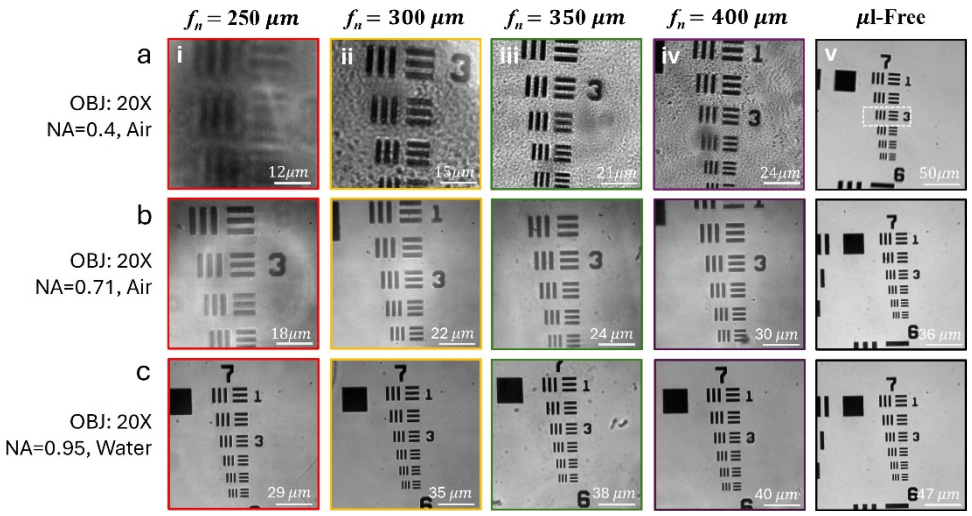


**Fig. 6.** Optical performance of parabolic microlenses (Ø = 600 μm) coupled in virtual configuration to microscope objectives of increasing NA. The wide-field images of a USAF 1951 (group 7) resolution test chart were obtained through a single parabolic microlens with $f_n$ values of 250, 300, 350, and 400 μm, as well as without microlenses ($\mu L$-Free) when coupled directly to a 20x objective lens: (a) a low NA (0.4) dry objective, (b) a high NA (0.71) dry objective and (c) a high NA aperture (0.95) water immersion objective. The defocused image observed when the NA = 0.4 microscope objective was coupled to microlens $f_n$ = 250 μm (panel (a-i)) is due the effective focal plane falling at a shorter distance than the thickness of the USAF glass substrate. The overall magnification, $M_{tot}$, varies according to the relative position of microlenses and objective lens. Shown in the figure are the conditions of maximum magnification for the three objective lenses used.

The magnification of the acquired images can be computed (see Table 4) as the product of the magnification of the objective lens and the microlens (see Materials and methods, section

Optics EXPRESS

2.7). We can verify that a higher magnification can be achieved from the system with lower NA microscope objective, reaching even a 3.85x value for the $f_n$ = 300 μm lens. When microlenses were coupled to a higher NA objective lens (NA = 0.71 and 0.95), all acquired images through microlenses showed lower magnification (Table 4) but a higher image sharpness (Fig. 6(b) and (c)). These measurements demonstrate the remarkable optical performance and capability of microlenses in achieving images with higher magnification than the coupled microscope objective, with similar or improved sharpness.

**Table 4. The microlenses magnification evaluated on wide-field images of the USAF 1951 target[a]**

| | Parabolic Microlenses $f_n$ (μm) | | | |
|---|---|---|---|---|
| Objective Lens | 250 $M_{\mu l}$ | 300 $M_{\mu l}$ | 350 $M_{\mu l}$ | 400 $M_{\mu l}$ |
| 20x, NA = 0.4, Dry | | 3.85X | 2.3X | 1.87X |
| 20x, NA = 0.71, Dry | 2.8X | 2.09X | 1.95X | 1.7X |
| 20x, NA = 0.95, Water | 1.3X | 1.24X | 1.22X | 1.21X |

[a]The microlenses magnification was evaluated using wide-field images of the USAF 1951 target (horizontal line element of 3, group 7), acquired through microlenses. The microlenses were coupled to low- and high-numerical aperture objective lenses.

To fully assess the imaging potential of the lenses, we studied their behavior also for fluorescence wide-field imaging, again in virtual configuration. We used a water solution of 10 μm fluorescently labeled (Nile Red) polystyrene beads and a fixed sample of a section from the plant *Convallaria Majalis*. To do so, parabolic microlenses ($f_n$ = 350 μm) were coupled to a 20x dry (NA = 0.35) objective lens in a wide-field optical microscope and the epifluorescence images at the glass coverslip focal plane (Fig. 7(a,b)) and through one microlens (Fig. 7(c,d)) were collected and compared. We could retrieve the magnified fluorescence images of beads through the microlenses resulting in a magnification ≃1.9, that leads to total magnification $M_{tot} = M_{\mu l} M_{obj} \simeq 1.9 \times 20 \simeq 38$. Fig. 7(a)-(c) indicates that the images are not affected by large aberrations in the middle of the field of view (≃200 μm). Out-of-axis optical aberrations arise at the edge of the lens (Fig. 7(a)-(c)), where the beads away from the optical axis tend to assume an elongated shape and to appear out-of-focus. This behavior can be ascribed to a combination of astigmatism and field curvature and could be related to lens curvature [42]. Nevertheless, these aberrations are not present in the center of the lens, preserving the 200 μm FOV.

For the fluorescence wide-field imaging of *Convallaria Majalis*, the microlenses were coupled to a 10x dry (NA = 0.25) objective lens (Fig. 7(e)). When properly positioned, the image of this sample was also obtained through the microlens (Fig. 7(f)), resulting in a high magnification ≃4.5, which leads to a total magnification $M_{tot} = M_{\mu l} M_{obj} \simeq 4.5 \times 10 \simeq 45$. The high-quality magnified epi-fluorescence images of fluorescent beads and *Convallaria Majalis* demonstrate the excellent optical performance capabilities of microlenses in fluorescence wide-field imaging mode. In conclusion, the experiments confirm the high optical quality of these lenses for both transmission and epifluorescence wide-field imaging and their potential applicability to future *in-vivo* imaging experiments. It is particularly noteworthy that our novel quasi-parabolic shape is sufficiently simple to provide high quality refractive lenses for a wide range of effective focal lengths, without the need to optimize the surface parameters for the specific needed value of NA, as for more traditional aspheric lenses [43].

Optics EXPRESS

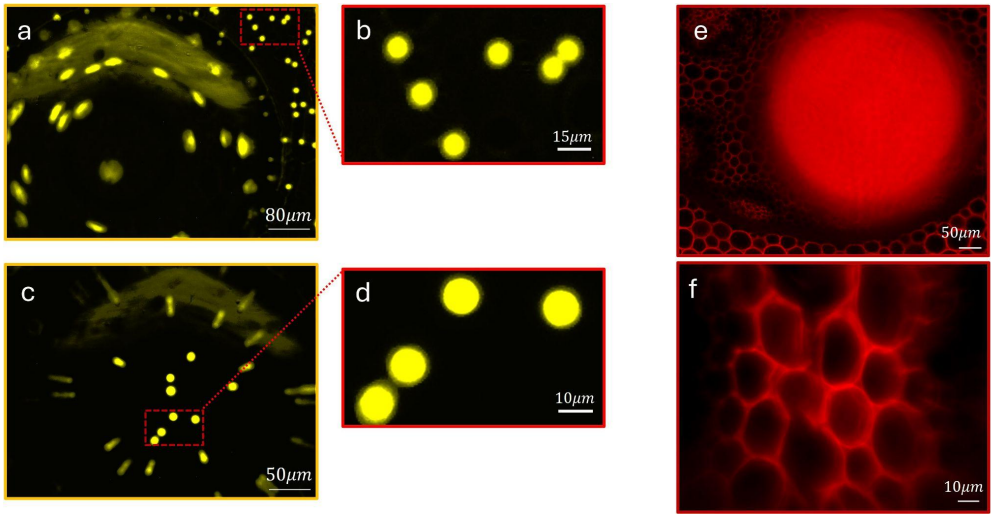


**Fig. 7.** Wide-field images of Nile red fluorescent beads and Convallaria Majalis using parabolic microlenses (Ø = 600 μm, $f_n$ = 350 μm) coupled to a wide-field optical microscope. Images are obtained under green excitation and epifluorescence detection. (a) Control wide-field image of the beads when the objective focal plane is set to the glass coverslip. In this condition the beads outside the lens FOV (in the upper right-hand area) are imaged in-focus by the objective alone, whereas through the lens the beads appear out-of-focus (central area). (b) a close-up of the region highlighted in red in (a). (c) Wide-field image of the beads collected in-focus through the microlens. (d) Close-up of the region marked in red in (c), where a total magnification equal to 38X has been achieved. (e, f) Wide-field images of Convallaria Majalis under green excitation. (e) Epifluorescence image obtained while focused on Convallaria out of the lens. The central circular signal corresponds to the out-of-focus signal collected by the microlens. (f) Wide-field image collected through microlenses.

## 3. Materials and methods

### *3.1. Sample preparation for two-photon polymerization*

The photoresist used to structure the microlenses was the SZ2080, which is a negative hybrid organic-inorganic UV-curable resist that is biocompatible and extensively used for biological applications. SZ2080 is composed by 20% of zirconium (Zr) and 80% of silicon. 1% of Irgacure-369 (2-Benzyl-2-dimethylamino1-(4-morpholinophenyl)-butanone-1, n. 405647 from Merck, EU) is added to the resist as photoinitiator to increase the efficiency of the polymerization. The photoresist was drop-casted on a 12 mm diameter circular glass coverslip with a thickness between 170 and 230 μm (#1.5, Menzel-Glaser, Germany) under a chemical hood. A control amount of 46 μl liquid SZ2080 photoresist was deposited with a volume pipette (Pipetman 100 G, Gilson). The samples were left under the chemical hood for 48 hours to allow the photoresist to dry by solvent evaporation. Once the material condensed, the photoresist reached a semi-solid state to prevent any unwanted sliding of the structures during the fabrication process, making it suitable for further laser-induced polymerization. The photoresist appears transparent before and after polymerization.

### *3.2. Two-photon laser polymerization setup*

In this work, the 2PP fabrications were performed using a custom-built setup. Suppl. Fig. S7.1 shows the schematic of the 2PP fabrication system. It consists of a femtosecond Ytterbium (Yb)

Optics EXPRESS

fiber laser ($\lambda$= 1030 nm, 1 MHz, with minimum pulse duration = 230 fs, Satsuma, Amplitude System). The output power reaches a maximum value of 10 W. The fabrication of parabolic microlenses was performed with $\lambda$ = 1030 nm, 1 MHz repetition rate, 230 fs pulse duration, and a laser power ranging from 19 to 22 mW. The laser beam passes through a series of mirrors steer it to a 2x telescope and finally to a half-wave plate coupled to a polarizer. The half-wave plate is mounted on a software-controlled motorized rotator that allows the dynamic control of the power during 2PP fabrication (MPS50GR-TTM-G80-DC-LMO-PLOTS, Aerotech, USA). At the end of the optical path, the beam is tightly focused by an objective (100x, Water immersion, with NA = 1.1, Nikon, Japan) directly onto the SZ2080 photoresist. We used an aluminum rectangular custom-made container to hold the sample, connected to a gimbal mechanical system (Gimbal Mounts 100, Thorlabs). The sample holder-gimbal complex is screwed on a planar (X,Y) translation stage (ANT130-035-L-ZS, Aerotech, USA) stabilized through two air-compressed pneumatic pistons. The software managing the movement of the three axes is Automation 3200 CNC Operator Interface, manufactured by Aerotech in the USA. It also controls the rotation of the half-wave plate. Additionally, the software is equipped with a feedback position and velocity control system that has a resolution of around 200 nm. To monitor the writing process in real-time and the polymerization process, a red-light emitting diode illumination is placed in the empty central cavity of the gimbal, under the sample holder-gimbal complex. A CCD camera was also mounted behind a dichroic mirror (Thorlabs, Germany). The optical path components and three translational stages are mounted on a granite table from Zali Precision Granite Technology (Italy). The outer surface of each single parabolic microlens was written by 2PP directly focusing the laser beam into the photoresist droplet. The sample was moved at a speed of 1 mm $s^{-1}$ reduced to 0.4 mm $s^{-1}$ at the end. Due to laser radiation absorption, the average power used for 2PP of the microlenses depends on the SZ2080 droplet thickness thus ranging from 17 to 20 mW (onto the objective entrance pupil). The power was gradually reduced at a height of 1 μm from the top of the microlens by 1 mW.

### 3.3. Sample development and UV exposure

After the 2PP process, the samples underwent development to remove the unpolymerized resist surrounding the microfabricated structures. Briefly, the samples were soaked for 30 min in a glass beaker filled with a 50% v/v 2-pentanone, 50% v/v isopropyl alcohol solution (Sigma–Aldrich, USA). Afterward, a few drops of isopropyl alcohol were used to cautiously wash the samples which were then gently dried by room temperature Nitrogen. Afterward, the samples were exposed to 300 mW of UV irradiation ($\lambda$ = 385 nm, LIGHTNINGCURE LC-L1V3 UV-LED from Hamamatsu) for 360 seconds in 3 steps of 120 seconds each to crosslink the unpolymerized inner core of the microlenses. The exposure process was performed illuminating through the glass substrate to avoid direct and additional exposure of the previously polymerized surface. The process was optimized to achieve structural stability without causing resin degradation, taking into account the radiation intensity and exposure time's strong dependence on the substrate thickness, the volume of photoresist to be polymerized, and the shape of the lens. It consisted of three phases, each exploiting a different angle of exposure of the UV lamp with respect to the glass horizontal plane: 0°, -45°, and +45°, (Fig. 2(b)) to fully crosslink the entire parabolic volume of the microlenses to achieve stability.

### 3.4. SEM sample preparation and imaging

The parabolic microlenses were sputter-coated with either 60 nm of conductive protective coating (Electra 92 – Allresist), or with a 15 nm gold layer (Anatech Hummer 6.2), as shown in Fig. 2(c), and Fig. 3(a, b) respectively. The images were acquired using a LEO 1525 SEM (Zeiss, Germany) equipped with a field emission gun. The SEM images of the samples were obtained by collecting secondary electron (SE) signals, with the microscope working at an acceleration voltage of 5

Optics EXPRESS

kV and with an Everhart–Thornley detector. Prior to the SEM analysis, the microlenses were sputter-coated for 30 s at 15 mA using Au as a target, resulting in a 15 nm thick film.

### 3.5. Optical profilometer

Qualitative surface analysis of fabricated microlenses was performed using an optical profiler-Filmetrics Profilm3D (manufactured by Filmetrics, California) along the z-axis in steps of 5 µm, covering a total length of 101 µm over an area of $229 \times 172$ µm$^2$. In each acquisition, 560 profile points in X-axis and 350 points in Y-axis were collected, applying white light interferometry. The surface profile and roughness of the fabricated microlenses were measured on the Profilm3D profilometer with a Nikon 50x DI objective at a 2x zoom setting. The lens surface was scanned, and the distance of profile points was 350 nm. The average roughness parameter, $R_a$ , was estimated from the average $R_a$ of the line profile using the following formula [44], $R_a = \frac{1}{N}\left(\sum_{i=1}^{N} |Z_i|\right)$ where N is the number of data points of the array in the horizontal direction and Z is the surface height relative to the reference mean plane [45].

### 3.6. Optical characterization

To test the minimum spot size under collimated beam illumination, we used a custom-made optical setup for optical characterization. Figure 4(a) with three laser sources: 473 nm (SLIM-473 CW Monolithic DPSS laser, GMP, Zurich), 532 nm (green laser, class IIIb, OPTICAL UNIPHASE), and 638 nm (TLS001-635, Thorlabs driven by a red single-mode optic fiber P1-630A-FC-1, Thorlabs). In the optical path, microlenses are mounted on a three-axis support, allowing for adjustment of the microlenses in front of the incident collimated laser beam. The configuration was adapted to measure the intensity distribution of a Gaussian beam, which was focused on parabolic microlens. The tube lens (f = 150 mm) and CCD camera sensor (DMK33UX183) are aligned to accept rays from infinity. Images of the intensity profile were then collected at various distances along the optical axis through a microscope objective (16x, NA = 0.25, f = 11 mm) as shown in Fig. 4(b). We did not observe changes in the optical properties of the lenses when using them for several months, thus demonstrating their stability in time.

### 3.7. Wide-field imaging

Transmitted light images of the 1951 USAF target (Fig. 6) have been acquired by a custom-made upright microscope. It is based on a wide-field illumination, obtained by means of a white LED source (400-700 nm wavelength range, Thorlabs, Germany) and collimated by a condenser lens (f = 50 mm, Thorlabs, Germany). The detection has been performed by means of both a low NA objective (Plan N, 20x, NA = 0.4, dry immersion, Olympus, Japan) and a high NA objective (XLUMPlanFI, 20x, NA = 0.95, water immersion, Olympus, Japan), as specified in the caption of Fig. 6. Finally, a tube lens with a focal length of 200 mm (Thorlabs, Germany) allowed projecting the transmitted light on an intermediate plane, where a CMOS camera with pixel size = 5.3 µm (UI-3240CP-M-GL, IDS, Germany) has been placed for the image collection. In order to calculate the magnification due to the microlens alone, $M_{\mu l}$, we first measured the dimension of a horizontal line element 3 in group 7 ($D_{free-\mu l}$) using images taken without microlenses (Fig. 6(a), (b), and c-v). Then, we measured the dimension of the horizontal line element 3 in group 7 ($D_{\mu l}$) using images taken through each microlens. Afterward, we divided the dimension obtained with microlenses ($D_{\mu l}$) by that obtained without microlenses ($D_{free-\mu l}$) (Table 4). Fluorescence (Fluo) images of Nile red fluorescent beads were obtained using an inverted light microscope (Leica DMI3000 M, Germany) equipped with a 12 V/100 W halogen lamp, which includes an adjustable field diaphragm, adjustable aperture diaphragm, and 3-step oblique light for illumination. The images were acquired, while the microlenses were coupled to a dry objective (Plan N, 20x, NA = 0.35, PH1) in the microscope. Images were captured by

Optics EXPRESS

exciting in green (through a band pass filter 560/40 nm) for Nile red fluorescent beads, and epifluorescence emission was collected at 595 nm (through a band pass filter 610/75 nm). For *Convallaria Majalis* epifluorescence imaging, the microlens were coupled to (Plan N, EPI, 10x, NA = 0.25, Leica), excited in green, and collected in red.

## 4. Conclusion

In summary, we have presented the design, fabrication, and validation of high-NA and high FOV aspherical quasi-parabolic microlenses with 600 µm diameter, featuring adjustable focal lengths tailored for wide-field imaging in reflection and in fluorescence. The fact that the proposed sag function depends only on a single parameter yet allowing to correct the major aberrations over a FOV of about 200 µm and magnifications up to 40, must be considered as a substantial improvement with respect to the conventional second order aspheric lenses. Additionally, the structure of these single-element microlenses is simple enough that their *in-vivo* implantation with minimal inflammatory response of the hosting tissue can be envisaged. The quasi-parabolic microlenses are fabricated using a hybrid approach that combines a gray scale 2PP for crafting the microlens surface with subsequent 3D UV crosslinking to stabilize the internal structure. A complete optimization of the process was performed to minimize fabrication time and preserve the structures' robustness, obtaining excellent surface smoothness and optical quality for the lenses. Multimodal characterization was performed to carefully test the geometry of the produced microlenses. The optical performance of microlenses was explored in numerical simulation and experimentally in linear excitation mode. We successfully retrieved magnified epifluorescence and transmission wide-field images through microlenses coupled to a wide-field microscope with low, and high numerical objective lenses. The results demonstrate the potential imaging capability of these novel design high-NA quasi-parabolic microlenses in linear excitation mode. Furthermore, these single lenses are wide enough to provide a FOV of approximately 200µm, comparable to the FOV obtained on confocal and non-linear excitation microscopes and can be adapted for non-linear excitation imaging as well.

**Funding.** European Commission (EU, FET-OPEN project IN2SIGHT, G.A. 964481); European Research Council (ERC, call ERC-AdG-2021, project BEACONSANDEGG, G.A. 101053122).

**Acknowledgments.** We are grateful to Dr. Elisa Sogne for her valuable support in SEM imaging, and to Polifab for providing the SEM and optical profilometer devices. Funded by the European Union. Views and opinions expressed are, however, those of the authors only and do not necessarily reflect those of the European Union or the European Research Council. Neither the European Union nor the granting authority can be held responsible for them.

**Disclosures.** The authors declare no conflicts of interest.

**Data availability.** Data underlying the results presented in this paper are available from the corresponding author upon reasonable request.

**Supplemental document.** See Supplement 1 for supporting content.

## References

1. T. E. Matthews, M. Medina, J. R. Maher, *et al.*, "Deep tissue imaging using spectroscopic analysis of multiply scattered light," Optica **1**(2), 105–111 (2014).
2. P. Bianchini, G. Zanini, and A. Diaspro, *Label-free pump&probe nanoscopy*, V. Astratov ed, (Springer Nature, 2019) chap.7.
3. V. N. Astratov, Y. B. Sahel, Y. C. Eldar, *et al.*, "Roadmap on Label-Free Super-Resolution Imaging," Laser Photonic Rev. **17**(12), 2200029 (2023).
4. C.J.R. Sheppard, "Multiphoton Microscopy: a personal historical review with some future prediction," J. Biomed. Opt. **25**(01), 1–11 (2020).
5. N. Ji, "Adaptive optical fluorescence microscopy," Nat. Methods **14**(4), 374–380 (2017).
6. P. Pozzi, D. Gandolfi, C. A. Porro, *et al.*, "Scattering compensation for deep brain microscopy: The long road to get proper images," Front. Phys. **8**, 26 (2020).
7. C. L. Smithpeter, A. K. Dunn, A. J. Welch, *et al.*, "Penetration depth limits of in vivo confocal reflectance imaging," Appl. Opt. **37**(13), 2749–2754 (1998).

Optics EXPRESS


8. R. K. Pal, N. E. Kurland, C. Wang, *et al.*, "Biopatterning of silk proteins for soft micro-optics," ACS Appl. Mater. Interfaces **7**(16), 8809–8816 (2015).
9. S. Bianchi, V.P. Rajamanickam, L. Ferrara, *et al.*, "Focusing and imaging with increased numerical apertures through multimode fibers with micro-fabricated optics," Opt. Lett. **38**(23), 4935 (2013).
10. M. Marini, A. Nardini, R. Martínez Vázquez, *et al.*, "Microlenses Fabricated by Two-Photon Laser Polymerization for Cell Imaging with Non-Linear Excitation Microscopy," Adv. Funct. Mater. **33**(39), 2213926 (2023).
11. D. Wu, S.Z. Wu, L. G. Niu, *et al.*, "High numerical aperture microlens array of close packing," Appl. Phys. Lett. **97**(3), 031109 (2010).
12. P. I. Diethric, R. J. Harris, M. Blaicher, *et al.*, "Printed freeform lens arrays on multi-core fibers for highly efficient coupling in astrophotonic systems," Opt. Express **25**(15), 18288–18295 (2017).
13. R. Guo, S. Xiao, X. Zhai, *et al.*, "Microlens fabrication by means of femtosecond two photon photopolymerization," Opt. Express **14**(2), 810–816 (2006).
14. M. Vaezi, H. Seitz, and S. A. Yang, "A review on 3D micro-additive manufacturing technologies," Int. J. Adv. Manuf. Technol. **67**(5-8), 1721–1754 (2013).
15. L. Siegel, S. Ristok, and H. Giessen, "Complex aspherical singlet and doublet microoptics by grayscale 3D printing," Opt. Express **31**(3), 4179–4189 (2023).
16. L. Pertoldi, V. Zega, C. Comi, *et al.*, "Dynamic mechanical characterization of two-photon-polymerized SZ2080 photoresist," J. Appl. Phys. **128**(17), 175102 (2020).
17. J. Mačiulaitis, M. Deveikyte, S. Rekštyte, *et al.*, "Preclinical study of SZ2080 material 3D microstructured scaffolds for cartilage tissue engineering made by femtosecond direct laser writing lithography," Biofabrication **7**(1), 015015 (2015).
18. M. Malinauskas, A. Žukauskas, V. Purlys, *et al.*, "Femtosecond laser polymerization of hybrid/integrated micro-optical elements and their characterization," J. Opt. **12**(12), 124010 (2010).
19. Z. Y. Hu, H. Ren, H. Xia, *et al.*, "Two-Photon Polymerization Nanomanufacturing Based on the Definition–Reinforcement–Solidification (DRS) Strategy," J. Lightwave Technol. **39**(7), 2091–2098 (2021).
20. T. Gissibl, S. Thiele, A. Herkommer, *et al.*, "Sub-micrometre accurate free-form optics by three-dimensional printing on single-mode fibres," Nat. Commun. **7**(1), 11763 (2016).
21. T. Gissibl, S. Thiele, A. Herkommer, *et al.*, "Two-photon direct laser writing of ultracompact multi-lens objectives," Nat. Photonics **10**(8), 554–560 (2016).
22. H. Wang, W. Zhang, D. Ladika, *et al.*, "Two-Photon Polymerization Lithography for Optics and Photonics: Fundamentals, Materials, Technologies, and Applications," Adv. Funct. Mater. **33**, 221421 (2023).
23. J. Li, S. Thiele, R. W. Kirk, *et al.*, "3D-Printed Micro Lens-in-Lens for In Vivo Multimodal Microendoscopy," Small **18**(17), 2107032 (2022).
24. S. Thiele, C. Pruss, A. M. Herkommer, *et al.*, "3D printed stacked diffractive microlenses," Opt. Express **27**(24), 35621–35630 (2019).
25. F. Balli, M. Sultan, S. K. Lami, *et al.*, "A hybrid achromatic metalens," Nat. Commun. **11**(1), 3892 (2020).
26. S. Capuani, G. Malgir, C. Y. X. Chua, *et al.*, "Advanced strategies to thwart foreign body response to implantable devices," Bioeng. Transl. Med. **7**(3), e10300 (2022).
27. X. Zhou, R. A. Franklin, M. Adler, *et al.*, "Microenvironmental sensing by fibroblasts controls macrophage population size," Proc. Natl. Acad. Sci. U.S.A. **119**(32), e2205360119 (2022).
28. A. W. Lohmann, "Scaling laws for lens system," Appl. Opt. **28**(23), 4996–4998 (1989).
29. M. Khorasaninejad, W. T. Chen, R. C. Devlin, *et al.*, "Metalenses at Visible Wavelengths: Diffraction-Limited Focusing and Subwavelength, resolution Imaging," Science **352**(6290), 1190–1194 (2016).
30. J. R. Bumstead, J. J. Park, I. A. Rosen, *et al.*, "Designing a large field-of-view two-photon microscope using optical invariant analysis," Neurophoton. **5**(02), 1 (2018).
31. K. Ohki, S. Chung, Y. H. Ch'ng, *et al.*, "Functional imaging with cellular resolution reveals precise micro-architecture in visual cortex," Nature **433**(7026), 597–603 (2005).
32. A. Žukauskas, G. Batavičiute, M. Ščiuka, *et al.*, "Effect of the photoinitiator presence and exposure conditions on laser-induced damage threshold of ORMOSIL (SZ2080)," Opt. Mater. **39**, 224–231 (2015).
33. D. Gonzalez-Hernandez, S. Varapnikas, G. Merkininkaite, *et al.*, "Laser 3d printing of inorganic free-form micro-optics," Photonics **8**(12), 577 (2021).
34. A. Ovsianikov, J. Viertl, B. Chichkov, *et al.*, "Ultra-low shrinkage hybrid photosensitive material for two-photon polymerization microfabrication," ACS Nano **2**(11), 2257–2262 (2008).
35. H. E. Williams, Z. Luo, and S. M. Kuebler, "Effect of refractive index mismatch on multi-photon direct laser writing," Opt. Express **20**(22), 25030–25040 (2012).
36. J. C. Wyant, *White Light Interferometry* H. John Caulfield, ed. (SPIE, 2002) pp. 98–107.
37. M. Bouzin, G. Chirico, L. D'Alfonso, *et al.*, "Stimulated Emission Properties of Fluorophores by CW-STED Single Molecule Spectroscopy," J. Phys. Chem. B **117**(51), 16405–16415 (2013).
38. M. Born and E. Wolf, *Principles of Optics* (Pergamon Press, 2nd edition, 1964), Ch. IX.
39. D. Gonzalez-Hernandez, B. Sanchez-Padilla, D. Gailevičius, *et al.*, "Single-step 3D printing of Micro-optic with adjustable refractive index by ultrafast laser Nanolitography," Adv. Opt. Mater. **11**(14), 2300258 (2023).

Optics EXPRESS

40. M. Schmid, D. Ludescher, and H. Giessen, "Optical properties of photoresists for femtosecond 3D printing: refractive index, extinction, luminescence-dose dependence, aging, heat treatment and comparison between 1-photon and 2-photon exposure," Opt. Mater. Express **9**(12), 4564–4577 (2019).
41. M. Zhao, M. K. Chen, Z. P. Zhuang, *et al.*, "Phase characterization of metalenses," Light:Sci. Appl. **10**(1), 52 (2021).
42. R. Lin, E. T. Kipreos, J. Zhu, *et al.*, "Subcellular three-dimensional imaging deep through multicellular thick samples by structured illumination microscopy and adaptive optics," Nat. Commun. **12**(1), 3148 (2021).
43. G. I. Kweon and C. H. Kim, "Aspherical lens design by using a numerical analysis," J. Korean Phys. Soc. **51**(1), 93–103 (2007).
44. M. Chand, A. Mehta, R. Sharma, *et al.*, "Roughness measurement using optical profiler with self-reference laser and stylus instrument-A comparative study," Indian J. Pure Appl. Phys. **49**, 335–339 (2011).
45. L. Lesovoy, F. Matiko, and B. Chaban, "Equation of Arithmetic Mean Deviation of Roughness Profile," Energy eng. control syst. **5**(2), 81–88 (2019).